Research in Astron. Astrophys. **2013** Vol. **13** No. **8**, 961–977
http://www.raa-journal.org *http://www.iop.org/journals/raa*

Research in Astronomy and Astrophysics

Analysis of the coronal source of the partially limb-occulted flare on 2002 July 20 *

Jin-Hua Shen[1,2], Victor Melnikov[1,3], Tuan-Hui Zhou[1] and Hai-Sheng Ji[1]

[1] Key Laboratory for Dark Matter and Space Astronomy, Purple Mountain Observatory, Chinese Academy of Sciences, Nanjing 210008, China; *jihs@pmo.ac.cn*
[2] Graduate University of Chinese Academy of Sciences, Beijing 100049, China
[3] Central Astronomical Observatory at Pulkovo, Russian Academy of Sciences, Saint Petersburg 196140, Russia

Received 2013 January 16; accepted 2013 February 26

Abstract We carry out a detailed analysis of the X3.5 solar flare that occurred on 2002 July 20, which is the strongest partially limb-occulted flare ever observed by the RHESSI satellite. The main results are: (1) during the main impulsive phase that lasts $\sim$ 10 minutes, the motion of the thermal sources follows a U-shaped trajectory. Non-thermal sources move in a similar way, but in a series of larger zigzags. We further show that the non-thermal sources are actually leading the contraction motion. (2) During the main impulsive phase, X-ray sources at different energies continuously form a loop-like configuration, with the highest energy source (up to $\sim$ 100 keV) and the lowest energy source (down to $\sim$ 10 keV) being located at two ends. The entire loop-like configuration moves in a U-shaped trajectory, while keeping the order of descending energy from highest to lowest during motion. Two non-thermal hard X-ray sources with different energies are spatially well separated in the distribution. The unusual complexities of the X-ray emissions in the tenuous solar corona challenge interpretations using bremsstrahlung in a simple magnetic configuration.

Key words: Sun: activity — Sun: X-ray — Sun: flares

1 INTRODUCTION

During solar flares, a large amount of free magnetic energy is transformed into the acceleration of energetic particles (Miller et al. 1997). However, the mechanism for particle acceleration in solar flares is still not well understood. Hard X-ray (HXR) emission from solar flares is frequently analyzed to investigate the mechanism of particle acceleration, since HXR emission during solar flares is generally believed to be produced by high energy electrons via bramsstrahlung processes (Brown 1971). As bremsstrahlung emission is proportional to the ambient density, intense HXR sources generally appear at chromospheric footpoint regions (Hoyng et al. 1981). In the low density corona, HXR emission (coronal HXR source) is usually much fainter. When intense footpoint emission appears, coronal sources are very difficult to observe due to the limited dynamic range of current X-ray imaging telescopes. However, coronal HXR sources are of particular importance for

* Supported by the National Natural Science Foundation of China.

studying the mechanism of electron acceleration, since the location of the acceleration site is generally assumed to be located high in the corona. On the other hand, the mechanism for the production of HXR emission and even γ-ray emission from the low density corona is not well understood either (Chen & Bastian 2012). Hence, HXR observations made with the Reuven Ramaty High Energy Solar Spectroscopic Imager (RHESSI) (Lin et al. 2002) have attracted a new round of attention to coronal HXR sources in recent years (Krucker et al. 2008a and references therein).

For flares occurring just behind the solar limb, HXR footpoint emission can be completely occulted and coronal HXR emissions can be observed without being limited by the dynamic range of HXR imaging telescopes. Therefore, footpoint occulted flares are very valuable for studying the behaviors of thermal and non-thermal emissions in the corona. While the study of coronal HXR sources dates back to the early 1970s (e.g., Frost & Dennis 1971) and the era of the YOHKOH spacecraft (Kosugi et al. 1991; Tomczak 2001; Tomczak 2009), RHESSI, with its unprecedented high spatial, spectral and temporal resolution in HXR observations, has enabled a great deal of progress in this field (Krucker et al. 2008b; Krucker et al. 2010). For coronal HXR sources, the most frequently studied topic is the spatial relationship between thermal and non-thermal sources, like the above loop-top source reported and studied by Masuda et al. (1994). Previous studies usually assume a radial dependence or height dependence. However, we have seen that radial motion can be a special case (Shen et al. 2008; Veronig et al. 2006). Therefore, there is a strong possibility that a non-thermal source's position has an offset not only in the radial direction but also in longitude and latitude. This may be one of the reasons why later studies indicate that the Masuda flare is not typical, since at most times the projection effect will occur. In the same sense, when we accept the statistical survey made by Krucker et al. (2008b), who showed that thermal and non-thermal emissions are often co-spatial with each other, and at times, they can be separated by a few arcseconds, then we should be aware of the projection effect. From this point of view, we are able to understand why non-thermal sources are below thermal sources in some flares (e.g., see fig. 12 of Tomczak 2009).

Coronal HXR sources are often very weak, and thus HXR photons have often been roughly classified into two energy bands during previous investigations: thermal and non-thermal. Their spatial relationship is used to infer the mechanism of HXR emission and even the scenario of magnetic reconnection or particle acceleration. As is well known, a thermal X-ray source itself contains contributions from an energy band (e.g., from 10 to 30 keV), and so does a non-thermal HXR source. The spatial distribution of thermal sources at different energy bands gives a temperature structure and, thus, the direction of the thermal energy flow or the position of energy release. For non-thermal HXR sources at different energies, the previous results have usually assumed that they are co-spatial. For this, we need strong limb-occulted flares to provide detailed information.

In this paper, we analyze a partially occulted X3.5 flare that occurred on 2002 July 20. This flare is the most energetic partially occulted event ever observed by RHESSI. HXR emission is observed up to 200 keV. In particular, non-thermal high energy emission ($>$ 30 keV) lasts for more than 25 minutes. This provides us with an unprecedented opportunity to investigate the spatiotemporal relationship between thermal and non-thermal sources in the corona.

The paper is organized as follows. Observations and analysis are given in Section 2. In Section 3 we discuss the results, and conclusions are given in Section 4.

2 RESULTS

2.1 Temporal and Spectral Behaviors

The flare analyzed in this paper occurred on 2002 July 20, with the GOES soft X-ray (SXR) starting to increase around 20:00 UT. The flare occurred in the active region NOAA 10039, which produced many flares during its transit across the solar disk, including the famous γ-ray flare on 2002 July 23 (Lin et al. 2003). Extrapolating the flare's location from the time when AR 10039 was visible on the disk to the flaring time shows that the flare occurred about 15° behind the east limb from Earth's

perspective, corresponding to an occultation height of about 20 Mm in the radial direction. Thus, its HXR emissions purely originate from the corona. Despite the effective occultation, RHESSI recorded intense HXR emission up to >200 keV. From RHESSI's database, we find that it is the most energetic partially occulted flare ever observed by the satellite. Examining the history of X-ray observations of coronal sources for large flares, Orbiting Solar Observatory 5 (OSO-5) had detected X-rays up to 220 keV from a highly occulted flare (Frost & Dennis 1971), however, OSO-5 had no imaging capability. Therefore, the flare presented here deserves a thorough analysis.

The flare belongs to the class of long duration events; the SXR emission lasts for almost 10 hours. Figure 1 shows the X-ray and microwave light curves as observed by GOES, RHESSI and the Ovens Valley Solar Array (OVSA) (Gary & Hurford 1990). A GOES SXR time profile between 20:00 and 23:00 UT is plotted in Figure 1(a). Two RHESSI nights occurred during this time period. From the GOES light curve, we can see a long early rising phase (more than one hour) that precedes a later impulsive phase. During this period, ejections of material are seen in HXR and Hα, which are addressed in Section 2.2 of this paper. Figure 1(b)–(c) plots the HXR light curves obtained from RHESSI data in seven energy bands from 20:10 to 21:50 UT. From the RHESSI light curves, we can see that emissions $\leq$ 30 keV are much more gradual than emissions $>$ 30 keV. The different time profiles reflect the existence of two components in this flare: thermal and non-thermal (Krucker et al. 2007a). The time profiles for emissions $>$ 30 keV have two rounds of enhancement. The first round consists of one HXR peak characterizing the main impulsive phase of the flare ($\sim$ 21:05–21:15 UT). The second round apparently consists of three small HXR peaks, starting at about 21:27 UT. As we will see below, the peak from 21:33 to 21:37 UT (Fig. 1(c)) does not come from the flare's emission.

Figure 1(d) plots the light curves of microwave emission at 1.6 and 16.4 GHz, as observed by OVSA. OVSA's microwave observation covers 45 frequencies from 1 to 18 GHz with a cadence of 4 s. Unfortunately, we were not able to construct a map of the microwave emission for this flare (Lee J., private communication). Figure 1(d) shows that the microwave light curves show a good correlation with HXR emissions at higher energies ($>$ 30 keV), showing two rounds of enhancement. The second round of microwave emission is even stronger than the emission from the first round by nearly one order of magnitude, attaining 10^4sfu. The difference is due to the different emission mechanisms associated with HXR and microwave. Microwave non-thermal gyrosynchrotron emissions depend on many parameters including the strength of the magnetic field as well as the amount of mildly relativistic electrons, their energy spectral slope and anisotropy, trapping and accumulation efficiency, etc. (Fleishman & Melnikov 2003; Melnikov et al. 2002). From the comparison with the HXR light curves $>$ 30 keV, we find that the last HXR peak (Fig. 1(c), 21:33–21:37 UT) does not come from the Sun; rather it should arise from a perturbation caused by magnetospheric particles around the RHESSI satellite.

The time profiles of X-ray emission <30 keV (Fig. 1(b)) look similar to the GOES soft X-ray emission (Fig. 1(a)). However, as mentioned above, X-ray light curves >50 keV (Fig. 1(c)) show a good correlation with their microwave counterpart (Fig. 1(d)). Microwave emission arises from non-thermal gyrosynchrotron emission. From the light curves, the transition of energy between thermal and non-thermal X-ray emission can be estimated to be in the range of 30–50 keV. To precisely distinguish between thermal and non-thermal emissions, a spectral fitting to the X-ray emission is needed. During the second and third peaks (the second round of X-ray enhancement), HXR emission is contaminated by emissions from magnetospheric particles. We only create spectra during the period of the first peak ($\sim$ 21:06–21:19 UT), and assume a similar spectral behavior for the rest.

Figure 2 shows nine spectra, and the time for each spectrum is plotted in Figure 1(b) using vertical parallel lines. Most of the spectra are readily resolved into two components: thermal and non-thermal. After a number of tests, we find that a multi-thermal and broken power law with a fixed power law index of –1.5 below the break represents the data well. It is worth mentioning that, for some fittings, the value of chi-square arises mainly from the thermal fitting around 10 keV. The fitting results show that HXR emission above 40 keV can be safely regarded as non-thermal.

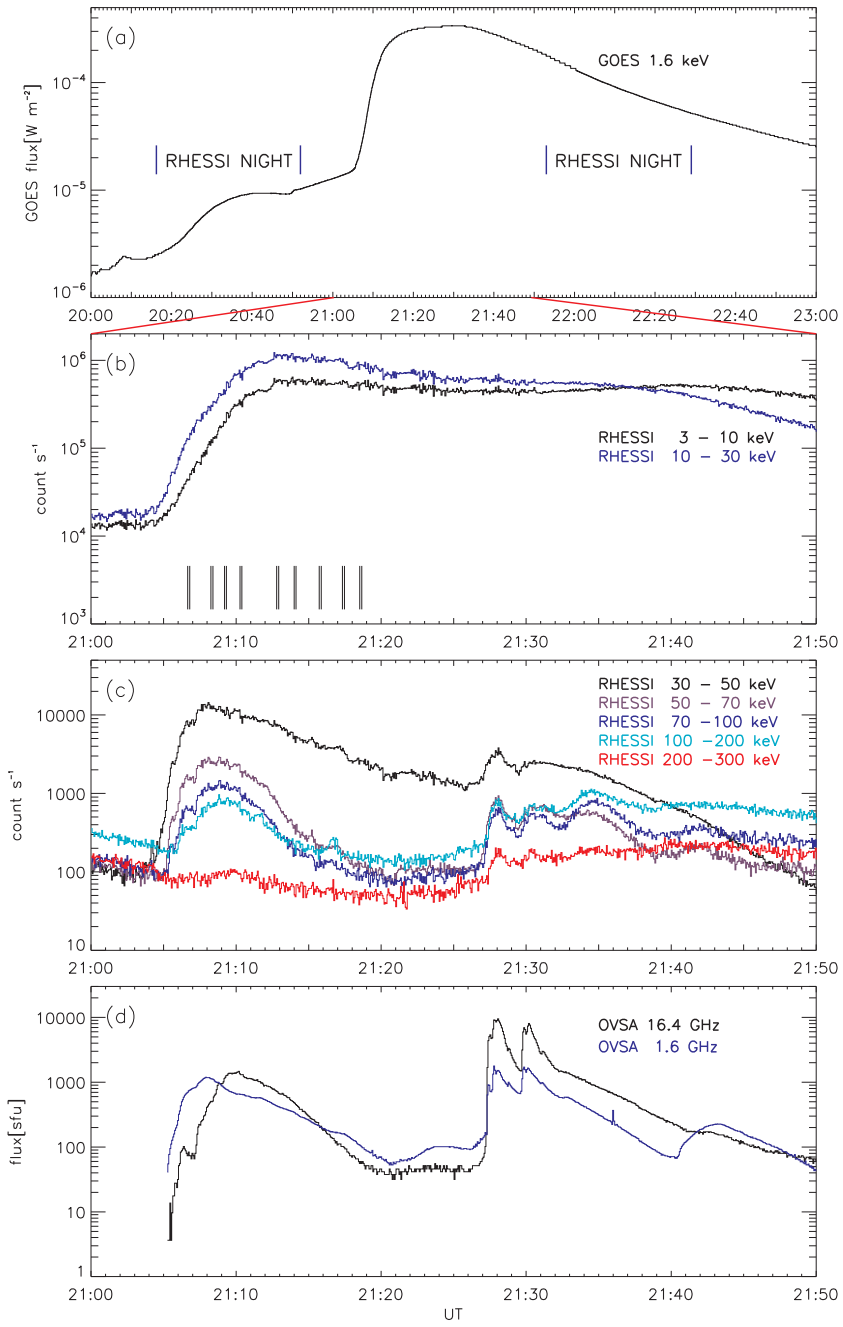

Fig. 1 X-ray and microwave time profiles of the 2002 July 20 flare. (a) GOES soft X-ray (1.6 keV) time profile from 20:00 to 23:00 UT. During this time period, two RHESSI nights occurred. (b+c) RHESSI hard X-ray time profiles at different energy bands during the period 21:00–21:50 UT. (d) Microwave time profiles from OVSA at 1.6 GHz (*blue*) and 16.4 GHz (*black*) during the same time period as panels (b) and (c). In the lower part of panel (b), nine pairs of vertical adjacent parallel lines show the positions of the nine time periods for the spectra in Fig. 2.

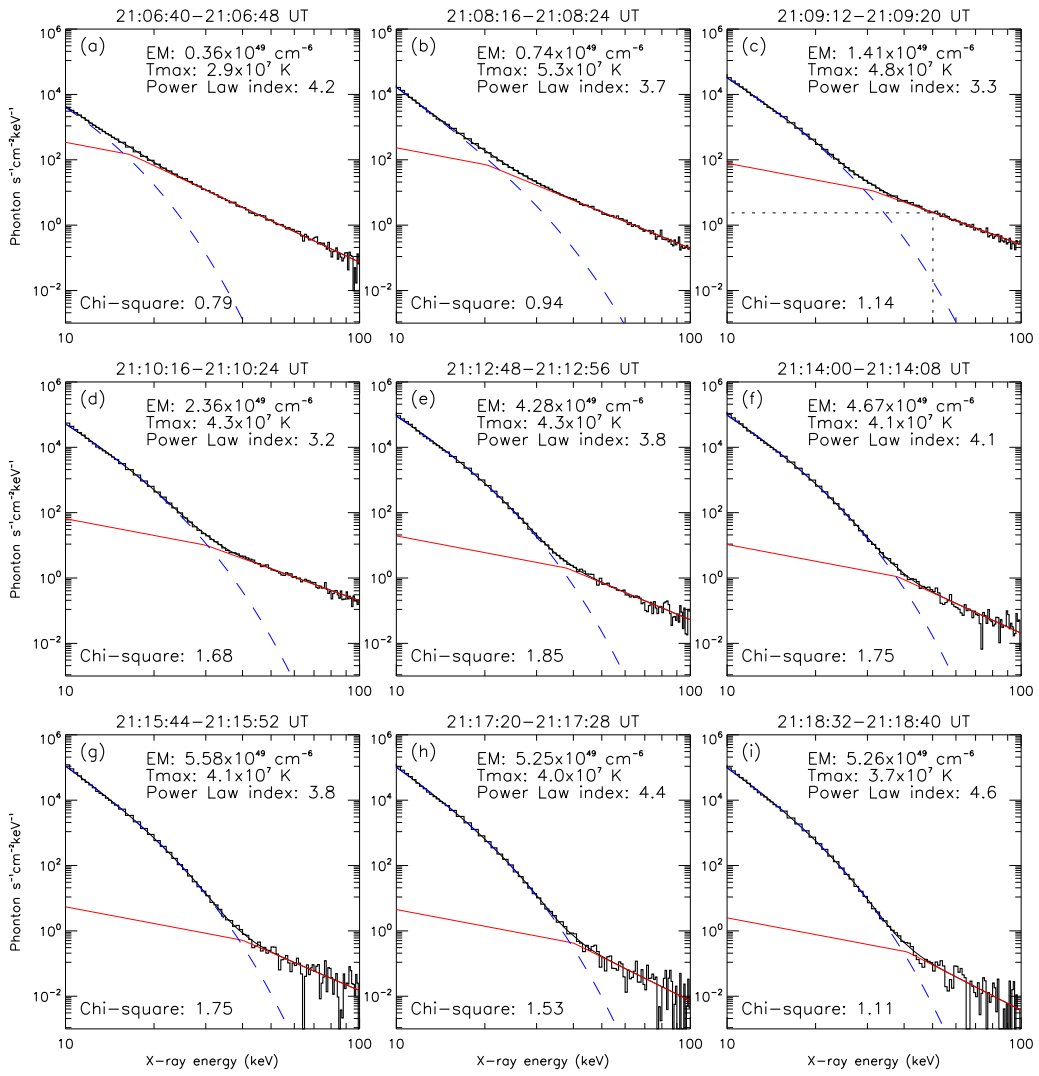

Fig. 2 Spectral fitting results during the nine time periods shown in panel (b) of Fig. 1. The data are shown as histograms, and the sum of all the fitted components is given as the solid black line. We can see that most of the spectra are clearly resolved into thermal and non-thermal components. The best explanation for each of the data is found to be a multi-temperature thermal fitting (*blue line*) plus a broken power-law fitting (*red line*).

Near the peak time of the flare, the flux at 50 keV is well above 1.0 photon s^{-1} cm^{-2} keV^{-1} from the two dotted lines in Figure 2(c). For occulted flares, either by observation or extrapolation, the flux at 50 keV is usually around 0.01 photon s^{-1} cm^{-2} keV^{-1} (Krucker et al. 2008b). Again, from a spectral point of view, this is an energetic partially occulted flare.

Figure 3 shows the temporal evolution of the spectral parameters during the main phase (21:05:36–21:15:00). Thermal emissions dominate below 30 keV and initially show the hottest tem-

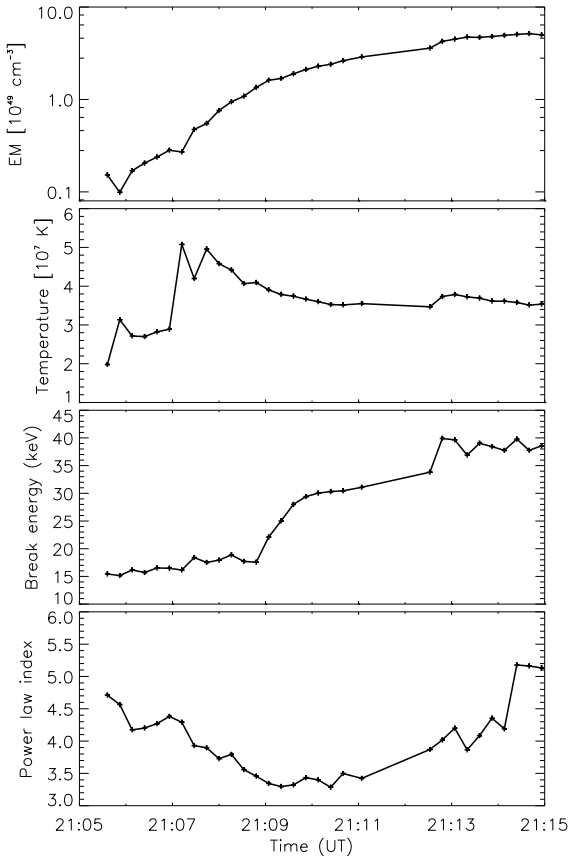

Fig. 3 Temporal evolution of the spectral fitting parameters in Fig. 2.

peratures, followed by slowly decreasing temperatures. The emission measures slowly increase with time. Compared to the statistical results for flares, this event is among those with flat or hard spectra. The spectral evolution behavior shows the usual soft-hard-soft pattern, and the breakup energy between the thermal and non-thermal sources slowly increases with time.

2.2 Hα and X-ray Jets during the Early Phase

This event was also observed by the EUV Imaging Telescope (EIT) at 195 Å (Delaboudinière et al. 1995) onboard the Solar and Heliospheric Observatory (SOHO) and full disk Hα telescope at the Big Bear Solar Observatory (BBSO). The full disk EUV and Hα observations show no emissions from the disk, confirming that the flare's footpoint emissions are fully occulted.

As stated above, from the GOES soft X-ray light curve, there is a slowly rising phase that lasts for more than one hour before the onset of the impulsive phase (Fig. 1(a)). During this phase several Hα ejections appear along parallel directions. The lower panels of Figure 3 give the temporal series of an Hα ejection during 20:09:37–20:17:37 UT. The ejection speed reaches 90 km s^{-1}. All Hα ejections fade away at certain heights. The information about the position of a BBSO image is obtained from an alignment with a continuum image taken by MDI onboard SOHO by visual sunspot matching. The accuracy of the alignment is estimated to be within $2''$. A RHESSI night

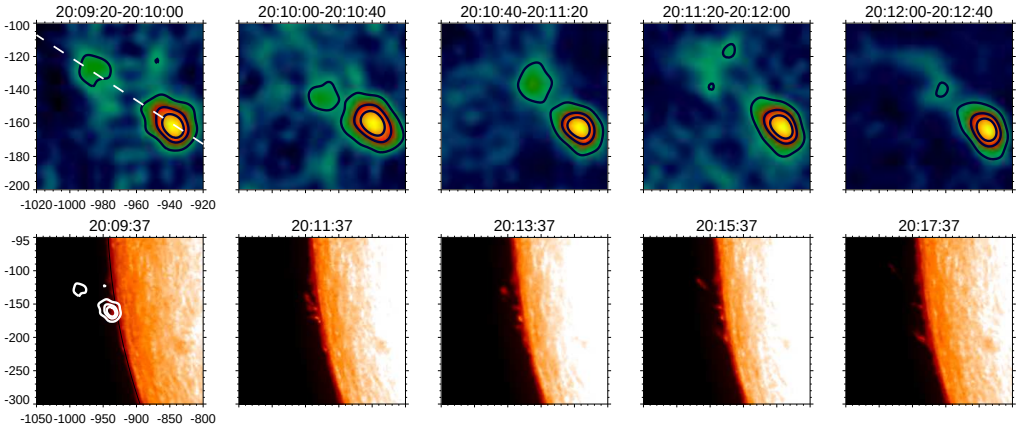

Fig. 4 *Upper panels*: a series of RHESSI maps showing an X-ray ejection (8–15 keV) during the slowly rising phase ($\sim$ 20:09–20:13 UT). The contour levels are the same for all time intervals, being 50%, 70% and 90% of each maximum emission. The white dashed line marks the axis of the ejection. *Lower panels*: Hα ejections during the slowly rising phase. On the first Hα map, contours of the X-ray emission correspond to the first X-ray map in the upper panels which are over plotted. Regarding the descending motion of the non-thermal sources, see Fig. 5 for more details.

occurs during this phase, however, we can still make some RHESSI maps before the night (upper panels in Fig. 4). RHESSI maps in the energy band 8–15 keV, which were obtained with the CLEAN imaging algorithm (Hurford et al. 2002), clearly show a small X-ray source being ejected from an elongated source. Because RHESSI is not a direct imaging instrument, the jet-like signature observed by RHESSI may correspond to an SXR jet. As we can see, the direction of the X-ray jet is along the direction of the Hα ejections.

2.3 U-shaped Trajectory of Thermal and Non-thermal Sources

The flare has sufficient counting statistics to make it possible to analyze the coronal HXR source with high temporal and spectral resolution. Firstly, we are interested in its motion during the flares. For the first time, we will show the motion of a non-thermal HXR source. For this purpose, we make CLEAN maps in the energy range 10–20, 20–30, 30–40 and 40–70 keV, with a time resolution of 16 s. From the results of spectral fitting in Figure 2, emission above 40 keV can be safely taken as purely non-thermal, especially during the rising phase. It should be pointed out that the coronal source is very complex. The emission sources are sometimes irregularly shaped and consist of double emission kernels. There is no standard way to define an exact location for such sources. Nevertheless, the concept of 'center of mass' (a centroid) is a statistically correct first order way to define the location of the irregularly-shaped sources. When a source is not a single source with a round shape, the position of the centroid is neither the site of maximum emission nor a symmetrical center. To add the weight of the maximum emission site, we measure the sources' centroid position within a contour level of 50%. For the value of the centroid itself, the error is within $1''$ (Hurford et al. 2002). Sometimes, the change in centroid values contains a contribution from the changes in the brightness distribution within the 50% contour. However, as we will see, the use of centroids can generally reflect the motion of the HXR sources in this flare.

The temporal series of centroid positions for the four energy bands is plotted in Figure 5. We can see that the motion of pure thermal sources follows a smooth U-shaped trajectory (Fig. 5(a)). We also

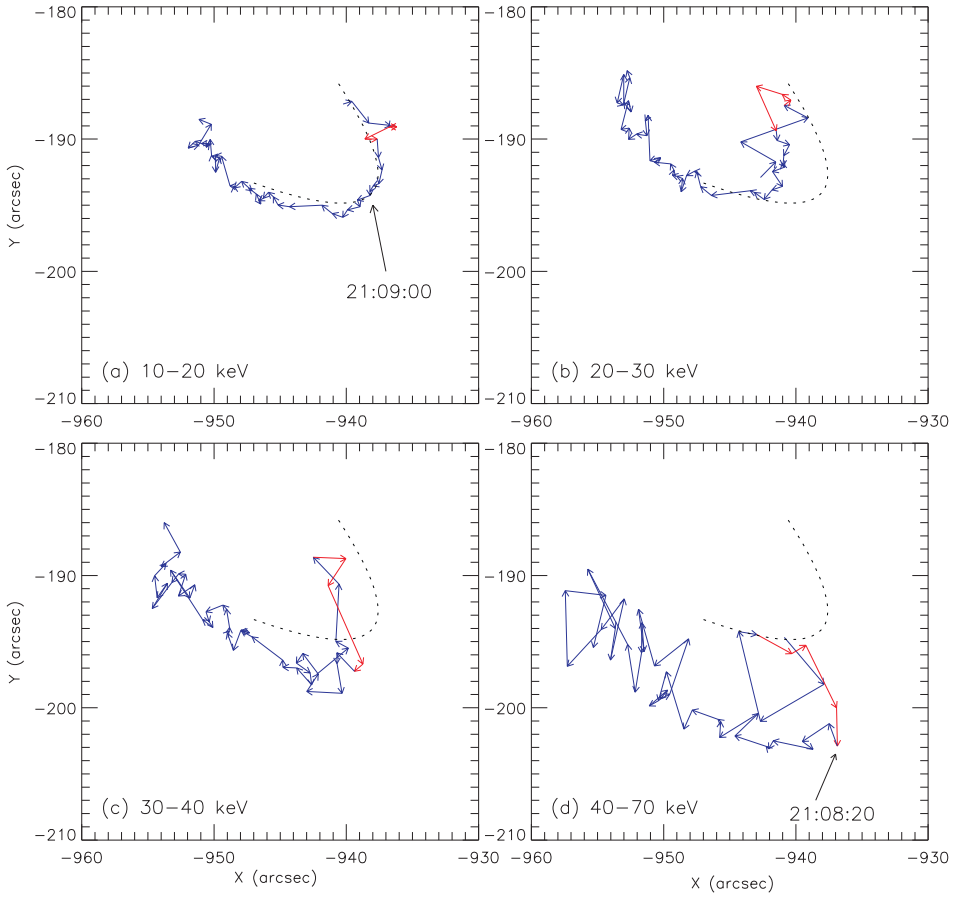

Fig. 5 Trajectories of the coronal sources at different energy bands. Arrows represent the direction of movement for the centroids. In each panel, a dotted U-shaped line fitting the smooth trajectory at 10–20 keV is shown. Four red arrows that correspond to the same time periods are specially drawn to show the obvious descending motion of the non-thermal HXR sources. Note that higher energy sources are actually leading the motion. This causes different times for the turning point of the U-shaped trajectories at different energy bands, e.g. $\sim$ 21:09:00 UT for 10–20 keV and 21:08:20 UT for 40–70 keV.

see that the centroids of non-thermal sources have larger fluctuations. Non-thermal sources move in a series of large zigzags, but a U-shaped pattern of motion can clearly be seen. Thus, we can say that the trajectories at all energies follow a U-shaped configuration. The timing for the turning point roughly corresponds to the peak time of the flare's main impulsive phase. The U-shaped trajectory can be associated with the "early contraction" and "later expansion" of flare loops (Shen et al. 2008). Loop contraction is generally seen as a continuous motion of thermal emission from higher to lower altitude for a few minutes followed by an increase in altitude that exceeds the initial starting point within a few minutes. Actually, for several of the coronal sources analyzed recently in the literature, we can see early descending motion followed by later ascending motion in altitude (e.g., Krucker et al. 2007a; Krucker et al. 2007b). It is worth noting that the motion is not in the radial direction at all.

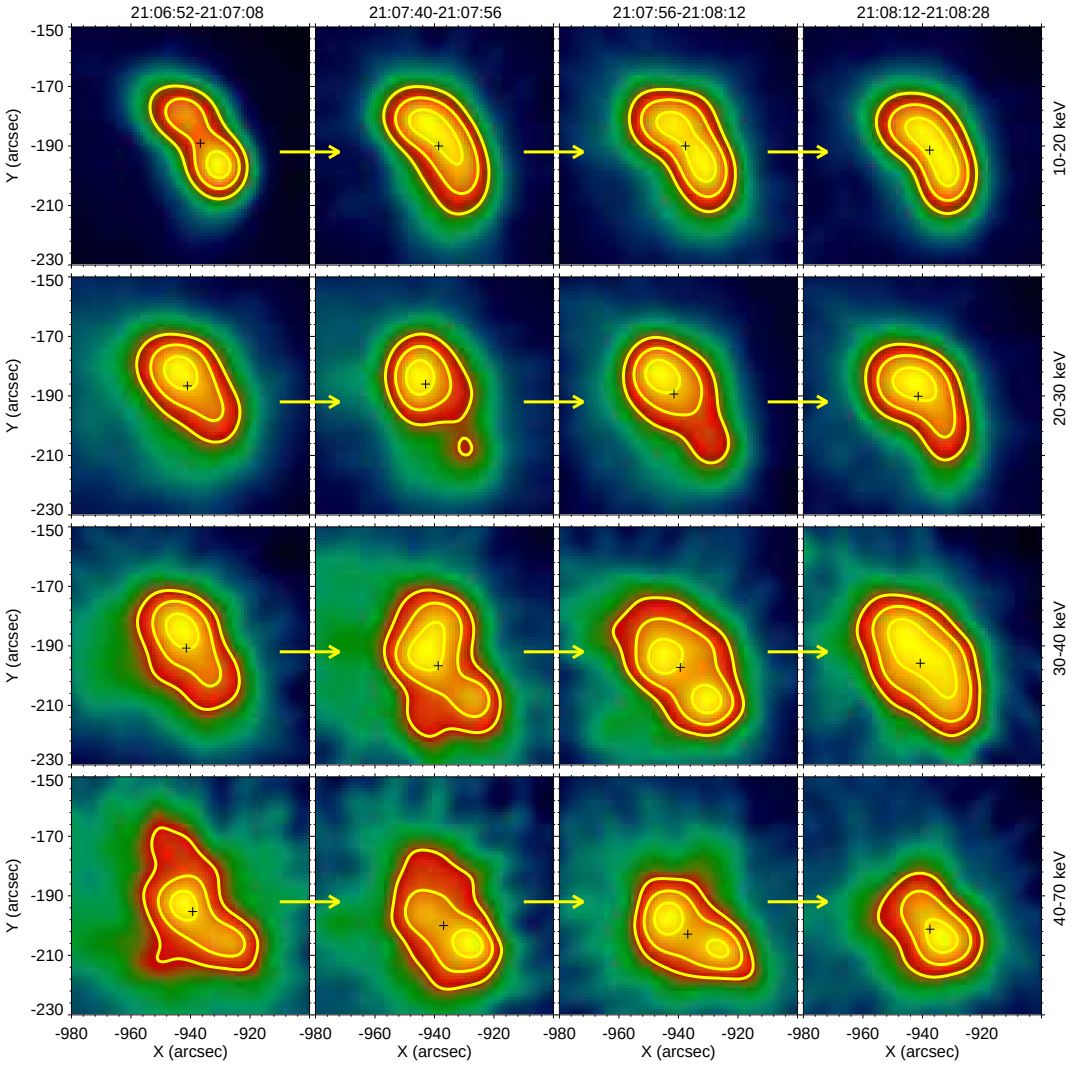

Fig. 6 HXR maps of four energy bands during four time periods. The four time periods are the same as the ones for the red arrows in Fig. 5. Contours are shown at 50%, 70% and 90% levels of each maximum emission. The yellow arrows show the direction of advancing time and the plus signs show the position of the computed centroids.

This is the first time that non-thermal HXR sources have been revealed to have a similar pattern of movement as the thermal sources. In Figure 5(d), four red arrows are specially drawn to show the obvious descending motion of the non-thermal part of the coronal source. The red arrows in all panels of Figure 5 correspond to the same time period. It is easy to note that higher energy non-thermal sources are setting the phase, i.e. non-thermal sources are actually leading the way during the U-shaped motion. This causes different times for the turning point of the U-shaped trajectories at different energy bands, e.g. $\sim$ 21:09:00 UT for 10–20 keV and 21:08:20 UT for 40–70 keV. Here, it is worth mentioning that the 2002 July 23 flare (homologous to this flare) has given us what appears

to be a new class of coronal HXR sources, namely coronal sources that precede the impulsive phase (Lin et al. 2003). This coronal source also has a U-shaped motion and a fixed temperature gradient. However, for this flare, little information can be found about the non-thermal part of the coronal source due to the appearance of intense non-thermal footpoint emission.

The U-shaped trajectory of the non-thermal sources is totally unexpected. For the sake of clarity, in Figure 6, HXR maps for the four energy bands during four time periods are plotted together for visual inspection. In Figure 6, the four time periods are the same as the ones for the red arrows in Figure 5. Contours are shown at 50%, 70% and 90% levels of each maximum emission. From the emission kernels and '+' signs (the position of computed centroids), it is clear that the $>$ 40 keV non-thermal source has the kind of descending motion depicted by the red arrows in Figure 4. This shows that the centroid obtained with the 'center-of-mass' method can be used to trace the motion of the HXR sources.

2.4 Spatial Distribution of Thermal and Non-thermal Sources

For a coronal source, what we are always interested in are the relative positions between the thermal and non-thermal sources. For this purpose, we make CLEAN maps in eight energy ranges with a time resolution of 16 s during the impulsive period of the flare (21:05–21:30 UT). The energy bands are 10–12, 12–14, 14–16, 16–20, 20–25, 25–30, 30–50, and 50–100 keV, respectively. For this study we use centroids computed in the same way as in Figures 4 and 5. A notable result is that the centroid positions of the non-thermal and thermal sources form a perfect continuous loop-like configuration during a number of time periods.

Figure 7 shows one example for the time period 21:08:12–21:08:28 UT. From Figure 7(a) we can see an obvious loop-like spatial distribution for centroids with different energies. Furthermore, the loop-like configuration is formed in order of descending energy, with the highest energy emission

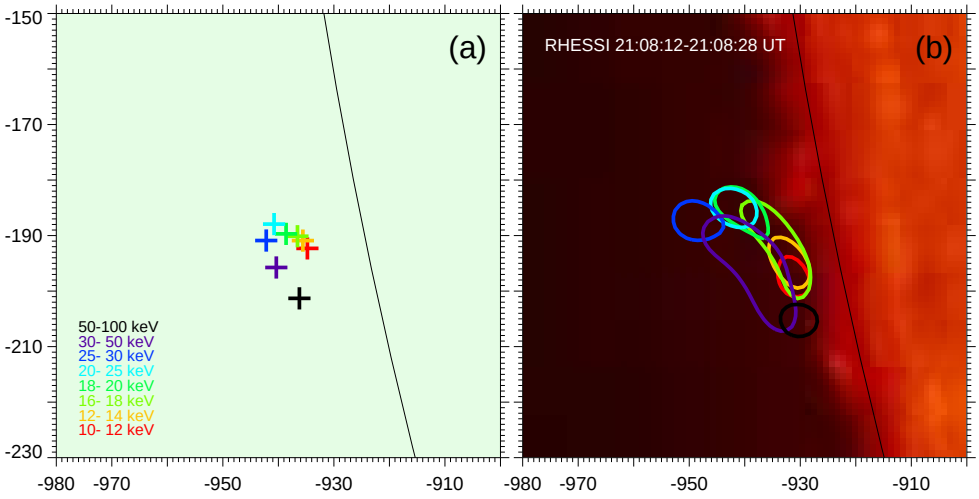

Fig. 7 A sample loop-shaped configuration of X-ray emissions at different energy bands during the period 21:08:12–21:08:28 UT. (a) The spatial distribution of the centroid positions of the sources at eight energy bands. (b) RHESSI contours overplotted on a simultaneous Hα image. The contour levels are at 95% of the maximum emission. The eight energy bands shown with different colors are listed in panel (a). The solid line shows the Sun's limb.

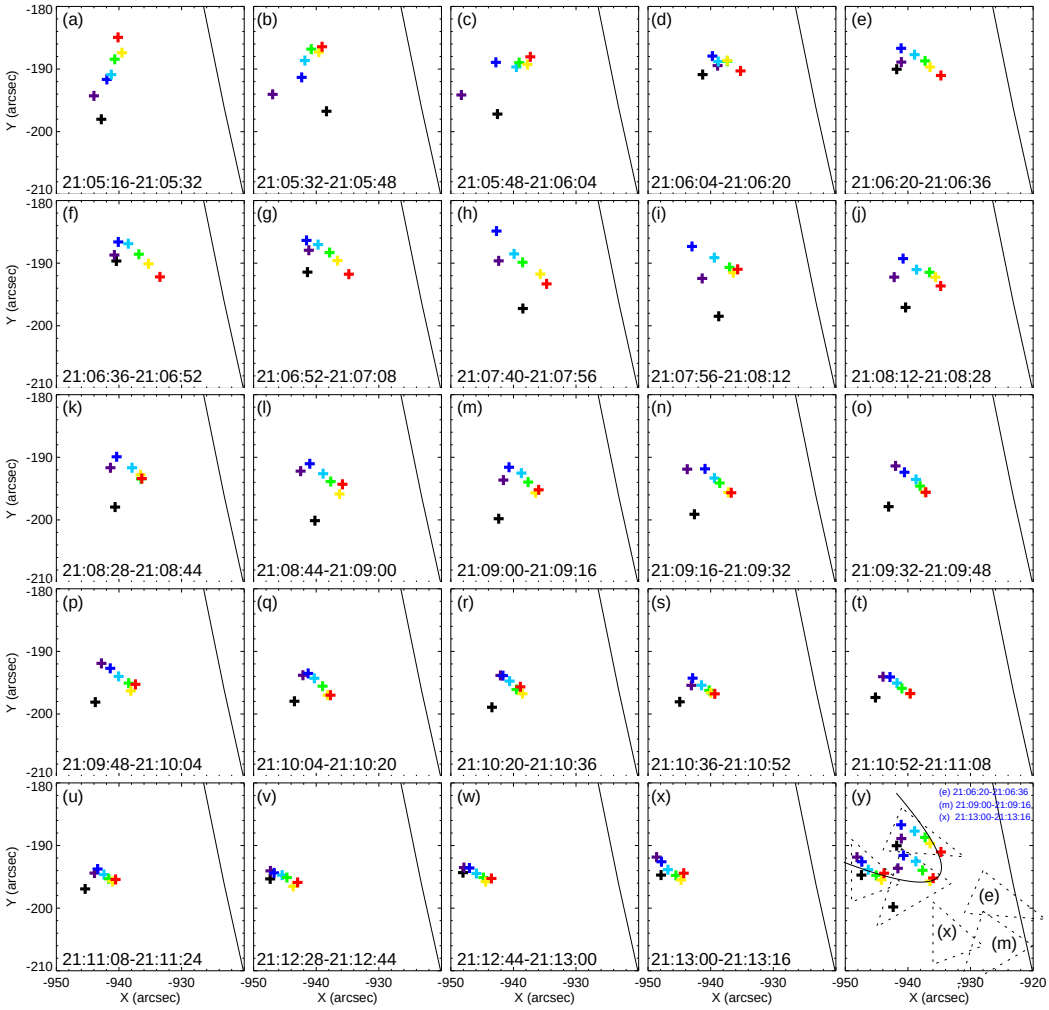

Fig. 8 Temporal evolution of the spatial configuration formed with the centroid positions (plus signs) of the coronal sources at eight different energies during the main X-ray peak phase (21:05:16–21:13:16 UT). The solid line shows the Sun's limb, and the colors represent different energy bands (cf. Fig. 6). The whole configuration follows a U-shaped motion, as depicted in panel (y).

sources (up to ∼100 keV) and the lowest energy sources (down to ∼10 keV) being located at two ends of the loop. The two legs are distributed with thermal and non-thermal sources, respectively. We plot 95% contours of the HXR emission at the eight different energy bands over a single map, as shown in Figure 7(b), and see a similar configuration for the spatial distribution. The loop-like spatial distribution is maintained for about seven minutes during the main impulsive phase.

Figure 8 plots the temporal evolution of the loop-like spatial distribution formed by the centroids of the HXR emission at the eight different energy bands during this time period. Apart from panels (a)–(d) and panels (v)–(x), the loop-like spatial distribution looks very solid. Actually, the whole configuration is moving, following the U-shaped path of contraction and expansion as re-

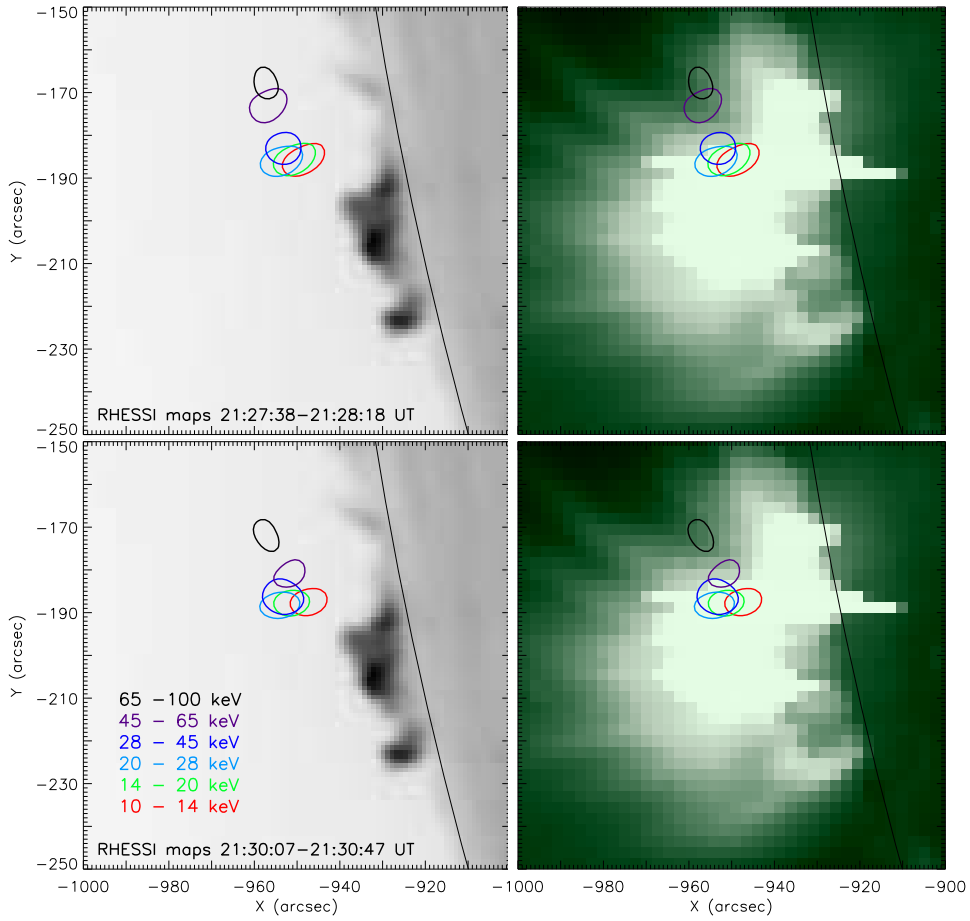

Fig. 9 The spatial configuration of X-ray emission in the context of Hα and EUV flare images at the later two peaks (cf. Fig. 1). Upper rows: contours at different energies (3–8, 8–12, 12–18, 18–28, 28–50, 50–100 keV) during the time period 21:27:38–21:28:18 UT. The contour levels are at 90% of the maximum emission. Lower rows: similar to the upper rows, but during the time period 21:30:07–21:30:47 UT.

ported above. Panel (y) of Figure 8 clearly shows this. During the motion, the order of descending energy in the loop-like distribution is maintained well. During the U-shaped motion, we can find that thermal sources always have a regular temperature structure, with the direction of the temperature gradient being fixed. Two non-thermal sources are spatially well separated and are always situated in one leg of the loop-like configuration. For example, during 21:09:00–21:09:16 UT, photons larger than 30 keV can be taken as non-thermal (see Fig. 2). During this period, the centroid positions for the 30–50 keV and 50–100 keV sources are separated by more than $5''$.

Figure 9 shows the spatial relationship between the non-thermal and thermal sources during the following two impulsive peaks. We did not record spectra during this period due to high level particle contamination from space. Nevertheless, non-thermal electrons appear with the strong microwave emissions (approaching 10^4 sfu) during this period as observed by OVSA (Fig. 1(d)). The thermal and non-thermal sources form a continuous spatial distribution in order of descending energy. The

configuration looks like what was reported by Masuda et al. (1994). The centroid of the 50–100 keV source (assumed to be non-thermal) is well above ($15''$) the thermal EIT flare loops. It is worth noting that the 50–100 keV source is situated in a dark notch region of the EUV emissions. Thus, the 50–100 keV source is definitely from a region with fewer thermal emissions and lower electron density. Compared with the Masuda source, there are two differences. (1) Thermal and non-thermal HXR sources form a continuous spatial distribution in order of descending energy. Two non-thermal sources are spatially well separated in the distribution. Here, we assume that HXR emissions larger than 45 keV are non-thermal. (2) The alignment of the distribution of HXR non-thermal and thermal sources is inclined to the north with respect to the vertical (radial) direction.

3 DISCUSSION

3.1 Coronal HXR Emission Mechanism in This Flare

In this investigation, we obtained the spatial relationship between thermal and non-thermal HXR sources and its temporal evolution. According to previous statistical results (Tomczak 2009; Krucker et al. 2008b), the spatial relationship between thermal and non-thermal HXR sources is highly diversified. The Masuda flare is very rare and not typical at all. For the coronal source of this flare, the most interesting feature is that the centroids of the thermal and non-thermal sources form a continuous loop-like spatial distribution. The loop-like configuration is formed in an exact order for energy with the highest energy emission sources (up to 100 keV) and the lowest energy sources (down to 10 keV) being located at the two ends of the loop. One leg is non-thermal and the other is thermal. The loop-like configuration remains for at least seven minutes, during which time the whole configuration has a U-shaped motion. Furthermore, two non-thermal sources with different energies are spatially well separated in the loop-like spatial distribution. During the two last HXR peaks, the results are similar except the spatial distribution forms in a nearly straight line, which may be taken as a special case for the loop-shaped configuration.

The contracting motion of thermal sources has been observed in a number of solar flares (e.g., Sui et al. 2004; Li & Gan 2005, 2006; Veronig et al. 2006; Joshi et al. 2009; Zhou et al. 2013; Liu et al. 2004; Ji et al. 2007). This is the first time that this kind of motion has been shown for non-thermal sources and may actually reflect the motion that indicates the site of particle acceleration.

As mentioned in the text, several images show double sources with the centroid appearing between the two sources. Mapping with longer time periods confirms the co-existence of the double sources. However, this may raise questions about using centroids to represent the position and motion of the sources. As we have seen in Figures 6 and 7, the contracting motion and loop-shaped configuration are real, as verified by a visual inspection. In fact, we carried out further analysis on the sources of a limb occulted flare that occurred on 2002 April 4. The reason for choosing this flare is that nearly all RHESSI X-ray sources associated with the flare are single ones with a round shape. The analysis gave similar results, and these will be included in a future paper on statistical analysis.

What is the mechanism that produces coronal HXR emissions in this flare? Let us first consider the thin-target model. In the thin target, energy losses for non-thermal electrons over a limited distance are negligible. Assuming a nearly constant plasma density along the loop, a beam of non-thermal electrons cannot produce well separated non-thermal HXR sources. Then we consider the thick target model. From the observed measure of thermal emission ($\sim 1.4 \times 10^{49}$ cm^{-3}) and the source volume ($\sim 9 \times 10^{27}$ cm^3, estimated from the FWHM area to the power of 1.5) at $\sim$ 21:09 UT, the density of the thermal source is of the order of 4.0×10^{10} cm^{-3}. To stop an electron with 100 keV of kinetic energy (which generates 50 keV HXR photons), a column density of 1.7×10^{21} cm^{-2} is needed. Under such a density, the equivalent length corresponds to $\sim 4 \times 10^{10}$ cm or 400 Mm. An effective trapping can produce this length scale, but special conditions are needed for the trapped electrons to produce the above-mentioned spatial distribution of HXR emissions at different energies. To find these conditions we need to numerically model an HXR spatial-energy distribution using the

kinetic Fokker-Planck equation for non-thermal electrons propagating in an inhomogeneous magnetic loop and being scattered due to Coulomb collisions (Reznikova et al. 2009) or wave-particle interactions (Petrosian & Donaghy 1999; Stepanov & Tsap 2002; Kontar et al. 2012).

In considering the mechanisms for HXR emission from solar flares, Korchak (1971) concluded that bremsstrahlung emission is favored in most cases but that inverse Compton scattering (ICS) could play a role if the ambient density in the source is low. In the framework of conceptual understanding, we can assume that the non-thermal part of the HXR emission in the spatial distribution is produced by the ICS of keV photons in the corona on a beam of relativistic electrons. During the process of scattering, electrons lose their energy and the scattered photons will have different energies. Here, it is worth noting that the non-thermal emission source (50–100 keV) in Figure 8 is situated in a dark notch region of EUV emissions. We argue that, in the EUV dark notch region, the EUV photons may have been converted to HXR photons via ICS. In this flare the existence of high energy EUV/SXR photons (keV) is not a problem. In addition, the existence of at least mildly relativistic electrons is also not a problem because of the presence at all stages of the flare of intense microwave emission (see Fig. 1(d)). It is known that mildly relativistic electrons producing microwaves are trapped and accumulated in abundance in the upper part of flaring loops (Melnikov et al. 2002). The loop-shaped spatial distribution of thermal and non-thermal sources is hard to reproduce, though conceptually, it may be produced by scattered electrons which keep changing direction during scattering, or it may be the result of the magnetic fields guiding particles. However, this would require a scattering optical depth close to one if it is caused by ICS, which is unlikely given the relatively low density of high energy electrons in the corona.

On the other hand, unlike small flares, the magnetic topologies of large flares are usually very complex, giving rise to a complex emission pattern that challenges simple interpretation. For this flare, we do not get an easy answer on the loop-like spatial distribution of HXR sources in order of descending energy from the bremsstrahlung mechanism. Also, the existence of two well separated non-thermal sources is very hard to explain in the framework of ICS. For ICS in solar flares, more observations and analysis are needed. A detailed quantitative estimation for the role of the ICS and bremsstrahlung mechanisms in this flare will be carried out in the following investigations (Chen, B., private communication).

3.2 Preferred Direction

We have seen that the contracting and expansing motions are not in the radial direction at all. The overall direction of movement is north-easterly (Fig. 5). The U-shaped trajectory forms at about 50° with respect to the eastern direction. For the thermal X-ray sources, their spatial distribution forms a temperature gradient that tells us the direction of energy flow. During the motion of the HXR sources, thermal sources are always aligned in a straight line and in order of descending energy (Fig. 8). Higher energy sources are located at a higher ‘height’ (Figures 5–6) along the expansion path. The statistical distribution representing the direction of the alined thermal sources (10–12, 12–14, 14–16 and 16–20 keV) shows that the direction of the alignment is northeastern and is in the range of 30°–40° with respect to the easterly direction during the main impulsive peak (Fig. 10). In addition, the direction of the X-ray and Hα ejections forms about 33° north of the easterly direction.

The preference for direction should reflect the basic framework for magnetic energy release in this flare. The pre-flare configuration and the evolution of the coronal magnetic field are very important for understanding the process of magnetic reconnection. EUV images are usually used as a tracer of the invisible magnetic fields.

Figure 11 shows a basic magnetic configuration before the flare. The good viewing angle permits us to clearly see the pre-flare magnetic configuration. We can see a magnetic loop (height: 30 Mm, span: 60 Mm, north of the dotted line in Fig. 11(a)) and an almost open field (south of the dotted line) inclined toward the magnetic loop. There is a dark lane (labeled by the dotted line in Fig. 11)

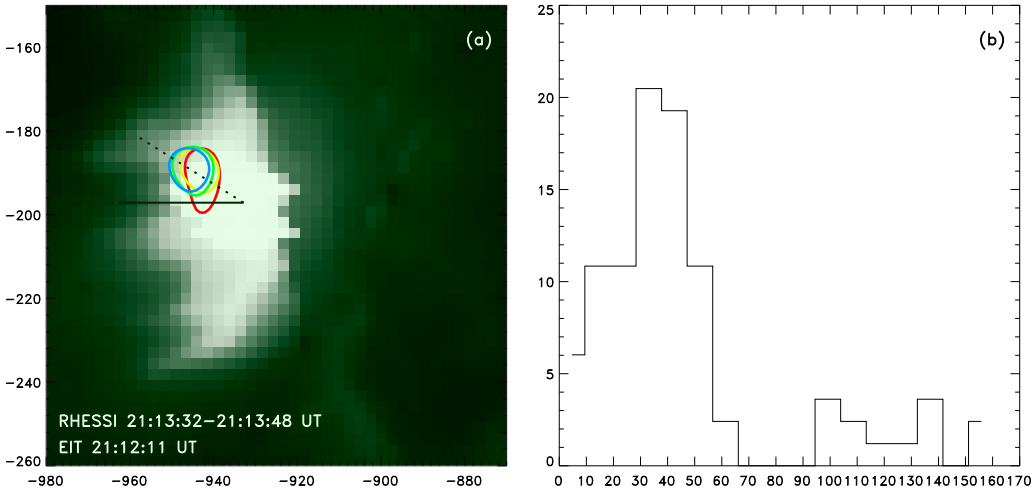

Fig. 10 (a) An EIT 195 Å image at 21:12:11 UT overlaid with contours (at the 90% level) of thermal X-ray emissions at four different energies (*red*: 8–10 keV, *yellow*: 10–13 keV, *green*: 13–16 keV, *blue*: 16–20 keV). The black solid line marks the east-west direction and the black dotted line fits the centroid positions of the thermal X-ray emissions at the four energy bands. The acute angle formed between the solid and dotted lines is defined as the direction of the temperature gradient. (b) The distribution (percentage) for the direction of the temperature gradient obtained during 83 time intervals (16 s) from 21:05:00 to 21:29:48 UT.

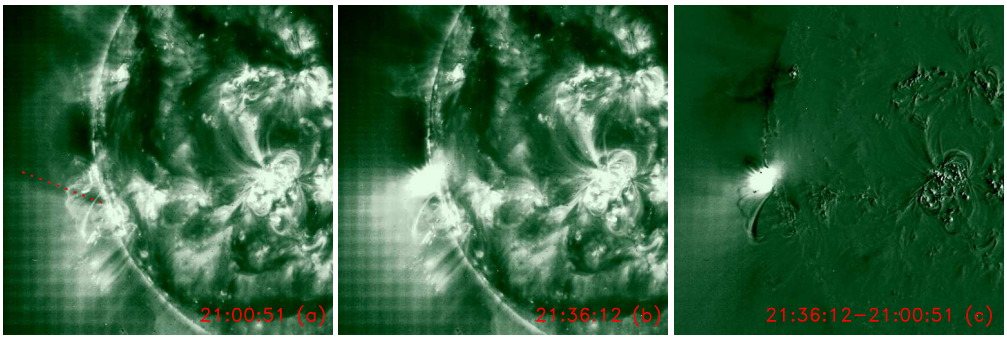

Fig. 11 EIT195 Å full disk images at 21:00:51 UT (a) and 21:36:12 UT (b) and their difference image (c). The red dotted line marks the location and direction of the dark lane between a magnetic loop and an open field that is inclined toward the loop.

between the magnetic loop and the inclined open field. The direction of the dark lane is 27° north of east. After the flare, part of the magnetic loop and the open field disappeared, as judged from a difference image between 21:12:11–21:00:51 UT (Fig. 11(c)). EIT 195 Å flaring loops appear near the dark lane region (Fig. 11(b)). The pre-flare 'magnetic' geometry and its evolution during the flare suggest that magnetic reconnection may have occurred in the dark lane region.

Table 1 List of Four Angles with Respect to East

Direction of the X-ray (Hα) ejections (Fig. 4)	$\sim 33^\circ$
Direction of the temperature gradient of thermal sources (Figures 8–10)	$\sim 30^\circ - 40^\circ$
U-shaped direction of movement for the X-ray coronal sources (Fig. 5)	$\sim 50^\circ$
Direction of the EUV dark lane (Fig. 11)	$\sim 27^\circ$

Now, we have directions for four types of different features. They are nearly parallel and follow a roughly similar direction (Table 1). This is the preferred direction for this flare. We propose that the preferred direction may reflect the direction of the current sheet, assuming that the dark lane is the magnetic separatrix layer (Demoulin et al. 1996), and hot and cool materials are ejected along the direction of the current sheet (Canfield et al. 1996).

4 SUMMARY

The X3.5 solar flare that occurred on 2002 July 20 is the strongest partially limb-occulted flare observed by RHESSI. Despite the occultation, an intense HXR emission is observed up to 200 keV. Near the peak time of the flare, the flux at 50 keV is well above 1.0 photon s^{-1} cm^{-2} keV^{-1}, two orders of magnitude larger than average. Importantly, the flare's non-thermal HXR emissions lasted for more than 20 minutes. Together with RHESSI's resolving power, the strong flare has given us a rare opportunity to carry out a detailed analysis of the spatiotemporal relationship between thermal and non-thermal coronal sources. Few partially occulted flares in history could allow researchers to conduct such a detailed study. After performing a comprehensive analysis, we find the following:

(1) Basically, the centroids of thermal and non-thermal HXR sources form a continuous spatial configuration that is distributed in order of descending energy. During the main impulsive phase, the configuration looks loop-like, with the highest energy source (up to $\sim$ 100 keV) and the lowest energy source (down to $\sim$ 10 keV) being located at the two ends. Most important of all, two non-thermal sources with different energies are well separated in the spatial distribution. The above features of HXR emission in the corona cannot be explained in the framework of the thin target and are difficult to explain with a thick target bremsstrahlung model.
(2) Both thermal and non-thermal sources (or the loop-like configuration) follow a U-shaped trajectory during the main impulsive phase. This can be taken as the signature of contraction and expansion. Higher energy non-thermal sources are actually leading the way during the U-shaped motion. This results in different times for the turning point of the U-shaped trajectory at different energy bands. Nevertheless, the timing for the turning point of the U-shaped trajectory roughly corresponds to the peak time of the flare. This is the first time that a non-thermal HXR source has been revealed as having an initial descending motion followed by a later ascending motion. It is likely that the site that produces energetic particles (the acceleration site) moves downward and upward with the contraction and expansion of the flare loops.
(3) During the flare, there is a strong preference for the direction of the temperature gradient derived from thermal X-ray sources at different energies between 10–20 keV, even though the sources are moving. The direction is found to be roughly parallel to: 1) the direction of the U-shaped motion, 2) the direction of the X-ray ejections during the initial slowly rising phase, and 3) the direction of a dark lane between the magnetic loop that later disappears and the nearby inclined open field. The four directions are northeasterly and form an angle of about 30°–50°from east. The preferred direction may reflect the direction of the current sheet.

Acknowledgements We are grateful to the anonymous referee who helped to improve the paper. We thank the teams at RHESSI, SOHO and BBSO for their efforts in obtaining and sharing the data. This

work is supported by the National Natural Science Foundation of China (Grant Nos. 11111120071, 10833007, 11173062, 11221063 and 11178002) and the National Basic Research Program of China (973 Program, 2011CB811402). VM is supported by the Chinese Academy of Sciences visiting professorship for senior international scientists (Grant No. 2010t2j36) and by the joint RFBR-CNSF (Grant No. 11-02-91175).

References

Brown, J. C. 1971, Sol. Phys., 18, 489
Canfield, R. C., Reardon, K. P., Leka, K. D., et al. 1996, ApJ, 464, 1016
Chen, B., & Bastian, T. S. 2012, ApJ, 750, 35
Delaboudinière, J.-P., Artzner, G. E., Brunaud, J., et al. 1995, Sol. Phys., 162, 291
Demoulin, P., Henoux, J. C., Priest, E. R., & Mandrini, C. H. 1996, A&A, 308, 643
Fleishman, G. D., & Melnikov, V. F. 2003, ApJ, 584, 1071
Frost, K. J., & Dennis, B. R. 1971, ApJ, 165, 655
Gary, D. E., & Hurford, G. J. 1990, ApJ, 361, 290
Hoyng, P., Duijveman, A., Machado, M. E., et al. 1981, ApJ, 246, L155
Hurford, G. J., Schmahl, E. J., Schwartz, R. A., et al. 2002, Sol. Phys., 210, 61
Ji, H., Huang, G., & Wang, H. 2007, ApJ, 660, 893
Joshi, B., Veronig, A., Cho, K.-S., et al. 2009, ApJ, 706, 1438
Kontar, E. P., Ratcliffe, H., & Bian, N. H. 2012, A&A, 539, A43
Korchak, A. A. 1971, Sol. Phys., 18, 284
Kosugi, T., Makishima, K., Murakami, T., et al. 1991, Sol. Phys., 136, 17
Krucker, S., Hannah, I. G., & Lin, R. P. 2007a, ApJ, 671, L193
Krucker, S., White, S. M., & Lin, R. P. 2007b, ApJ, 669, L49
Krucker, S., Battaglia, M., Cargill, P. J., et al. 2008a, A&A Rev., 16, 155
Krucker, S., Saint-Hilaire, P., Christe, S., et al. 2008b, ApJ, 681, 644
Krucker, S., Hudson, H. S., Glesener, L., et al. 2010, ApJ, 714, 1108
Li, Y. P., & Gan, W. Q. 2005, ApJ, 629, L137
Li, Y. P., & Gan, W. Q. 2006, ApJ, 644, L97
Lin, R. P., Dennis, B. R., Hurford, G. J., et al. 2002, Sol. Phys., 210, 3
Lin, R. P., Krucker, S., Hurford, G. J., et al. 2003, ApJ, 595, L69
Liu, W., Jiang, Y. W., Liu, S., & Petrosian, V. 2004, ApJ, 611, L53
Masuda, S., Kosugi, T., Hara, H., Tsuneta, S., & Ogawara, Y. 1994, Nature, 371, 495
Melnikov, V. F., Shibasaki, K., & Reznikova, V. E. 2002, ApJ, 580, L185
Miller, J. A., Cargill, P. J., Emslie, A. G., et al. 1997, J. Geophys. Res., 102, 14631
Petrosian, V., & Donaghy, T. Q. 1999, ApJ, 527, 945
Reznikova, V. E., Melnikov, V. F., Shibasaki, K., et al. 2009, ApJ, 697, 735
Shen, J., Zhou, T., Ji, H., et al. 2008, ApJ, 686, L37
Stepanov, A. V., & Tsap, Y. T. 2002, Sol. Phys., 211, 135
Sui, L., Holman, G. D., & Dennis, B. R. 2004, ApJ, 612, 546
Tomczak, M. 2001, A&A, 366, 294
Tomczak, M. 2009, A&A, 502, 665
Veronig, A. M., Karlický, M., Vršnak, B., et al. 2006, A&A, 446, 675
Zhou, T. H., Wang, J. F., Li, D., et al. 2013, RAA (Research in Astronomy and Astrophysics), 13, 526